











## Article

# Features of the Phase Preferences, Long- and Short-Range Order in $Ln_2(WO_4)_3$ ( $Ln = Gd, Dy, Ho, Yb$ ) with Their Relation to Hydration Behavior

Victor V. Popov <sup>1,2,\*</sup> , Yan V. Zubavichus <sup>3,\*</sup> , Alexey P. Menushenkov <sup>1</sup> , Alexey A. Yastrebtsev <sup>1</sup> , Bulat R. Gaynanov <sup>1</sup> , Sergey G. Rudakov <sup>1</sup>, Andrey A. Ivanov <sup>1</sup> , Fyodor E. Dubyago <sup>1</sup> , Roman D. Svetogorov <sup>2</sup> , Evgeny V. Khramov <sup>2</sup> , Nadezhda A. Tsarenko <sup>4</sup>, Nataliya V. Ognevskaya <sup>4</sup> and Igor V. Shchetinin <sup>5</sup> 

- <sup>1</sup> Department of Solid State Physics and Nanosystems, National Research Nuclear University MEPhI (Moscow Engineering Physics Institute), Moscow 115409, Russia; apmenushenkov@mephi.ru (A.P.M.); alexyastrebtsev@gmail.com (A.A.Y.); brgaynanov@gmail.com (B.R.G.); sgrudakov@mephi.ru (S.G.R.); andrej.ivanov@gmail.com (A.A.I.); walrus9f@gmail.com (F.E.D.)
  - <sup>2</sup> Kurchatov Synchrotron Radiation Source, National Research Center Kurchatov Institute, Moscow 123182, Russia; rdsvetov@gmail.com (R.D.S.); evxramov@gmail.com (E.V.K.)
  - <sup>3</sup> Synchrotron Radiation Facility SKIF, Boreskov Institute of Catalysis SB RAS, Koltsovo 630559, Russia
  - <sup>4</sup> JSC Design & Survey and Research & Development Institute of Industrial Technology, Moscow 115409, Russia; nadatsar@gmail.com (N.A.T.); ognevskayanv@mail.ru (N.V.O.)
  - <sup>5</sup> Material Science Department, National University of Science and Technology MISiS, Moscow 119049, Russia; ingvvar@gmail.com
- \* Correspondence: vvpopov@mephi.ru (V.V.P.); yvz@catalysis.ru (Y.V.Z.)



**Citation:** Popov, V.V.; Zubavichus, Y.V.; Menushenkov, A.P.; Yastrebtsev, A.A.; Gaynanov, B.R.; Rudakov, S.G.; Ivanov, A.A.; Dubyago, F.E.; Svetogorov, R.D.; Khramov, E.V.; et al. Features of the Phase Preferences, Long- and Short-Range Order in  $Ln_2(WO_4)_3$  ( $Ln = Gd, Dy, Ho, Yb$ ) with Their Relation to Hydration Behavior. *Crystals* **2022**, *12*, 892. <https://doi.org/10.3390/cryst12070892>

Academic Editors: Maria Milanova and Martin Tsvetkov

Received: 4 May 2022

Accepted: 17 June 2022

Published: 23 June 2022

**Publisher's Note:** MDPI stays neutral with regard to jurisdictional claims in published maps and institutional affiliations.



**Copyright:** © 2022 by the authors. Licensee MDPI, Basel, Switzerland. This article is an open access article distributed under the terms and conditions of the Creative Commons Attribution (CC BY) license (<https://creativecommons.org/licenses/by/4.0/>).

**Abstract:** The effect of synthesis conditions on the features of the long- and short-range order of  $Ln_2(WO_4)_3$  ( $Ln = Gd, Dy, Ho, Yb$ ) powders synthesized via coprecipitation of salts has been studied by a complex of physico-chemical techniques including synchrotron X-ray powder diffraction, X-ray absorption spectroscopy, Raman and infrared spectroscopy, and simultaneous thermal analysis. It was found that crystallization of amorphous precursors begins at 600 °C/3 h and leads to the formation of the monoclinic structure with sp. gr.  $C12/c1(15)$  for  $Ln_2(WO_4)_3$  ( $Ln = Gd, Dy$ ) and with sp. gr.  $P12_1/a1(14)$  for  $Ln = Yb$ , whereas crystallization of Ho precursor requires even higher temperature. After annealing at 1000 °C, the  $P12_1/a1(14)$  phase becomes the dominant phase component for all heavy lanthanoid types except for  $Ln = Gd$ . It was shown that the  $Ln$  ( $Ln = Dy, Ho$ , and  $Yb$ ) tungstates with the  $P12_1/a1(14)$  monoclinic structure correspond to trihydrates  $Ln_2(WO_4)_3 \cdot 3H_2O$  formed due to a rapid spontaneous hydration under ambient conditions. It was concluded that the proneness to hydration is due to a specific structure of the  $P12_1/a1(14)$  phase with large voids available to water molecules. Modifications in the local structure of  $Ln$ -O coordination shell accompanying the structure type change and hydration are monitored using EXAFS spectroscopy.

**Keywords:** lanthanoid tungstates; phase transitions; hydration; synchrotron XRD; X-ray absorption fine structure (XAFS); simultaneous thermal analysis; raman spectroscopy; FT-IR spectroscopy

## 1. Introduction

The lanthanoid ( $Ln$ ) tungstates present a wide group of inorganic complex oxides of transition metal and rare earth elements, which attract great interest both for basic science (great chemical flexibility, rich polymorphism and phase transformations, high ionic conductivity, etc.), and for practical uses (from electronics to biology) due to their multifunctional properties (optical, electronic, luminescence and so on) [1–4]. The most typical  $Ln$  tritungstates  $Ln_2(WO_4)_3$  with the 2:3 lanthanoid:tungsten atomic ratio have been known for many decades [5–7]. In particular, a considerable interest in the  $Ln_2(WO_4)_3$

tungstates is observed in the past few decades because these compounds exhibit negative thermal expansion (NTE) [8–11].

Nowadays, it is commonly accepted that a crystalline structure of  $Ln_2(WO_4)_3$  is governed by the ionic radius of the  $Ln^{3+}$  cation [7,9]. Light  $Ln$  ( $Ln = La-Eu$ ) tungstates from the first half of the rare-earth series at room temperature are characterized by a monoclinic structure (space group  $C12/c1$ ) in which the  $Ln^{3+}$  cation is eight-coordinated by the oxygen atoms. Meanwhile, heavier  $Ln$  ( $Ln = Gd-Dy$ ) tungstates from the mid of the series adopt at room temperature a monoclinic structure. These tungstates upon heating transform into an orthorhombic structure, which is reported to be intrinsically hygroscopic at room temperature. The heaviest  $Ln$  ( $Ln = Ho-Lu$ ) tungstates with smallest ionic radii are highly hygroscopic and form a stable orthorhombic trihydrate structure (sp. gr.  $Pnca$ ) at room temperature in which the  $Ln^{3+}$  cation is six-coordinated with the oxygen atoms [9].

However, some issues related to phase preferences of the  $Ln$  tungstates as well as exact boundary conditions of mutual phase transitions between them remain a subject of debate so far. The formation of light lanthanoid tungstates from La to Eu in their high-temperature modification was reported in [7]. This result contradicts to another report [9], where no high-temperature phase was found. According to numerous reports, the  $RE_2(WO_4)_3$  ( $RE = La-Ho$ ) family has modulated scheelite structure ( $\alpha$ - $Eu_2(WO_4)_3$ -structure of sp. gr.  $C12/c1$ ) at room conditions [12–18]. In the case of  $Ho_2(WO_4)_3$  there were some small peaks in its diffraction pattern, which belonged to the  $\gamma$ - $Sc_2(WO_4)_3$ —phase (hydrated at room conditions) [18]. It is generally accepted [19] that 1/3 of all sites within the  $Ln$  sublattice in the  $Ln$  ( $Ln = La-Ho$ ) tungstates with the imperfect scheelite-type structure remain unoccupied. The  $Ln$  vacancies tend to form an ordered superstructure at low temperatures, while statistically disordered structures tend to form upon heating. Xiao et al. [20] have shown that  $Ho_2(WO_4)_3$  has a monoclinic structure and is not hygroscopic. However, Lahoz et al. [21] reported the presence of a small fraction of the hydrated  $\gamma$ -phase in the structure of  $Ho_2(WO_4)_3$  crystals.

Neither lattice parameters nor atomic coordinates within the crystal structure of hygroscopic stable trihydrate  $Ln$  tungstates have been unequivocally determined so far. According to [9] the heavy  $Ln$  ( $Ln = Y, Er$  and  $Yb$ ) tungstates form the trihydrate orthorhombic  $Ln_2(WO_4)_3 \cdot 3H_2O$  at room temperature. On the other hand it was reported that  $Y_2(WO_4)_3 \cdot 3H_2O$  trihydrated phase can be indexed with a monoclinic cell ( $P2/m$ ) [8,22,23]. This monoclinic cell can be converted to a pseudo-orthorhombic phase, which is comparable to unhydrated orthorhombic phase at room temperature [8]. However, the mechanism responsible for the phase transition observed remains essentially unclear.

A detailed analysis of the literature data on the crystal structures and lattice parameters of heavy  $Ln$  tungstates is presented in Table S1.

An important information about the local structure features around W sites in  $Ln$  tungstates can be obtained with X-ray absorption fine structure (XANES and EXAFS) spectroscopy through the analysis of precise positions and relative intensities of W  $L_1$ -pre-edge peak and  $L_3$ -main edge [24,25] and non-linear curve fitting of coordination shells in EXAFS Fourier Transforms.

A lot of publications available in the literature describe properties of well-crystallized  $Ln$  tungstates prepared by the solid-state synthesis method [6,7,9,19,22]. This method requires the use of high calcination temperatures (usually  $\geq 1000$  °C) and long processing times (usually few tens hours) and cannot be used to monitor changes with the crystal structure during its emergence. In the present study, we apply another synthesis strategy, based on the calcination of precursor powders synthesized via the coprecipitation of respective salt mixtures [5,23,26,27]. This method is especially suitable to elucidate the stepwise evolution of overall crystallinity and phase transitions upon the emergence of well-crystallized material. It is realized by appropriate high-temperature treatments of the initially amorphous precursors at variable temperatures [28–30].

The aim of this work is thus to elucidate the influence exerted by synthesis conditions (including the type of the  $Ln^{3+}$  cation, calcination temperature, conditions of cooling and

subsequent storage time in air) on the long- and short-range order within  $Ln$  tungstates  $Ln_2(WO_4)_3$  ( $Ln = Gd, Dy, Ho, Yb$ ) synthesized via the coprecipitation followed by specific high-temperature treatments of the precipitated hydrated precursors. We apply a complex of physico-chemical methods, including synchrotron X-ray powder diffraction, XAFS spectroscopy, Raman and Fourier transform infrared (FT-IR) spectroscopies, supplemented by simultaneous thermal analysis. Earlier, we have successfully shown the potency of such multi-technique structural analysis of lanthanoid hafnates [28], zirconates [29,30], titanates [30], molybdates [31], light and intermediate  $Ln$  tungstates [32].

## 2. Experimental

### 2.1. Synthesis

The lanthanoid tungstates powders  $Ln_2(WO_4)_3$  were prepared by a reverse coprecipitation method similar to that reported in [23]. The starting chemicals  $Ln(NO_3)_3 \cdot xH_2O$  ( $Ln = Gd, Dy, Ho, Yb$ ) (the purity not lower than 99.95–99.99% and  $x = 4–6$  depending of  $Ln$  type) and  $Na_2WO_4 \cdot 2H_2O$  were purchased from CHIMMED (Moscow, Russia). The  $Ln(NO_3)_3$  aqueous solutions (0.1 mol/L) were dropwise poured into the  $Na_2WO_4$  aqueous solution (0.15 mol/L) at a rate of 9 mL/min at continuous intense stirring. The solutions of salt precursors were mixed in exact ratios required by stoichiometry, i.e.,  $Ln:W$  equals to 1:1.5. The aqueous suspensions obtained were characterized by a nearly neutral pH of 7–8. They were aged for an hour at room temperature to guarantee that the reaction is complete. The precipitates formed were filtered off, washed for several times with distilled water and then dried for 6 h at 80 °C. The dried precursors were then ground in an agate mortar to a fine powder and loaded into a muffle furnace LHT 02/16 (Nabertherm GmbH, Lilienthal, Germany). The powders were heated to specific temperatures in the range 500–1000 °C in air at a temperature ramp rate of 10 °C/min and kept at a constant temperature for 3 h. The annealed samples were either allowed to slowly cool to room temperature by unplugging the furnace or were quickly cooled (quenched) to room temperature by reloading from the hot furnace to the open air or a desiccator. The full list of samples studied is given in Table S2.

We adopted the following naming convention to denote samples under study. The first part of the codename corresponds to the chemical composition ( $LnWO$ , where  $Ln = Gd, Dy, Ho, Yb$ ). The second term indicates the calcination temperature used for the sample preparation (ranged from 500 °C to 1000 °C). Auxiliary conditions describing the preparation protocol are given in the third coding term (desic or repeat). Since the heavy  $Ln$  tungstates are intrinsically hygroscopic, the fourth coding term indicates the duration of their storage in air (from few minutes to 1.5 year). A detailed description of sample preparation and respective coding is given in Table 1.

**Table 1.** Synthesis conditions and symbols for  $Ln_2(WO_4)_3$  samples.

No	Preparation Protocol	Sample Code
1	$Ln_2(WO_4)_3$ precursors	$LnWO$ -prec
2	$Ln_2(WO_4)_3$ calcined at 1000 °C, cooled in the open air and then stored in air 1 day *	$LnWO$ -1000-1d
3	$Ln_2(WO_4)_3$ calcined at 1000 °C, cooled in a desiccator and then stored in air 1 day *	$LnWO$ -1000-desic-1d
4	$Ln_2(WO_4)_3$ calcined at 1000 °C, cooled in the open air, after that repeat heated up to 1000 °C, cooled in the open air and then stored in air 1 day *	$LnWO$ -1000-repeat-1d

\* Note: (1)  $Ln$  could correspond to either Gd, Dy, Ho or Yb depending on the synthesis protocol; (2) the calcination temperature varies depending on the specific example in a range of 500–1000 °C; (3) the storage time in air varies depending on the specific example from few minutes (min), days (d), weeks (w), months (m) to 1.5 years (1.5 y).

## 2.2. Characterization

The atomic emission spectroscopy with inductively coupled plasma (ICP-AES) was applied to quantify atomic ratios of metal cations in the freshly prepared precursors. ICP-AES measurements were performed using a Vista-PRO spectrometer (Varian Inc., Palo Alto, CA, USA).

The simultaneous thermal analysis (STA) of the powders, which implied thermogravimetry (TG) and differential scanning calorimetry (DSC) was performed with a SDT Q600 (TA Instruments, New Castle, DE, USA) analyzer over the range of temperatures of 30–1000 °C at a temperature ramp rate of 10 °C/min in the air atmosphere. To determine the water absorption rate all analyzed powders immediately prior to measurements were dried in a desiccator at 200 °C for 1 h. The kinetics experiments were conducted in air at a temperature of  $25 \pm 1$  °C and relative humidity of  $(60 \pm 5)\%$ . Changes in the mass of the samples were monitored with an analytical balance XS205DV (Mettler Toledo LLC, Columbus, OH, USA) with a nominal accuracy of  $1 \cdot 10^{-5}$  g.

The preliminary crystallographic analysis of the synthesized powders was done by X-ray powder diffraction (XRD) using a MiniFlex 600 in-lab diffractometer (Rigaku, Tokyo, Japan) with Cu  $K_{\alpha 1}$ -radiation ( $\lambda = 1.5406$  Å). More accurate structural information was gathered using synchrotron radiation-based X-ray powder diffraction (s-XRD) at the X-ray Structural Analysis beamline (Belok/XSA) of the Kurchatov Synchrotron Radiation Source (NRC Kurchatov Institute, Moscow, Russia) (the electron storage ring with the electron energy of 2.5 GeV and mean current stored of 100 mA). The incident radiation was monochromated to 0.8 Å (the photon energy 15,498 eV) using a Si(111) double-crystal monochromator. The X-ray beam spot size was about 400  $\mu\text{m}$  [33]. The synchrotron data acquisition was performed at room temperature in the transmission geometry using a SX165 CCD detector (Rayonix LLC, Evanston, IL, USA). The sample-to-detector distance was 150 mm. To extend the scattering angle range, the detector plane was tilted to 29.5°. The exposure time was 5 min. The polycrystalline reference powder LaB<sub>6</sub> NIST SRM 660a was used for the angular scale calibration. The Rietveld full-profile analysis was carried out using the JANA2006 software [34].

W  $L_1$ -edge (12,099.8 eV),  $L_3$ -edge (10,206.8 eV) and  $L_n$   $L_3$ -edges (from 7242.8 eV for Gd to 8943.6 eV for Yb) XAFS spectra were measured at the Structural Materials Science beamline at the Kurchatov Synchrotron Radiation Source (NRC Kurchatov Institute, Moscow, Russia) [35]. The measurements were done in the transmission geometry at room temperature. A Si(111) channel-cut monochromator was used for the energy scanning, which provided an apparent energy resolution  $\Delta E/E \sim 10^{-4}$ . Intensities of the X-ray beams before ( $I_0$ ) and after ( $I_1$ ) the samples were measured with ion chambers with appropriate N<sub>2</sub>/Ar mixtures. The  $k^2$  weighted normalized EXAFS function  $\chi(k)k^2$  was Fourier transformed over the  $k$  range of 2–14.5 Å<sup>−1</sup> (W  $L_3$ -edge) or 2–11 Å<sup>−1</sup> ( $L_n$   $L_3$ -edges). X-ray Absorption Near-Edge Structure (XANES) spectra were processed using the ATHENA software from the IFFEFIT data analysis package [36,37]. Extended X-ray Absorption Fine Structure (EXAFS) spectra were analyzed by means of non-linear curve fitting in the  $k$ -space using standard procedure [38] using the IFFEFIT and VIPER [39] data analysis packages. Photoelectron backscattering amplitudes and phase functions were determined ab initio with the FEFF9 code [40].

The Raman spectra were acquired with an inVia Qontor confocal Raman microscope (Renishaw plc, Wotton-Under-Edge, UK) at  $\lambda_1 = 532$  nm and  $\lambda_2 = 785$  nm over a wavenumber range of 50–2700 cm<sup>−1</sup> at a spectral resolution of 1 cm<sup>−1</sup>. A part of measurements was performed with a Nicolet iS50 FT-IR spectrometer (Thermo Fisher Scientific Inc., Waltham, MA, USA) with an auxiliary Thermo Scientific iS50 Raman unit ( $\lambda = 1064$  nm) at room temperature over a wavenumber interval of 100–3700 cm<sup>−1</sup> at a spectral resolution of 4 cm<sup>−1</sup>.

FT-IR spectra were recorded on a Nicolet iS50 FT-IR spectrometer (Thermo Fisher Scientific Inc., Waltham, MA, USA) equipped with a single reflection diamond module (ATR). IR spectra were collected over a wavenumber range of 400–4000 cm<sup>−1</sup> at a 4 cm<sup>−1</sup> resolution.

### 3. Results and Discussion

#### 3.1. ICP-AES Study

According to the synthesis protocol, the precipitates immediately formed as a result of the reaction between  $Ln^{3+}$  cations and tungstate anions ( $WO_4^{2-}$ ) as soon as reactants were mixed. ICP-AES measurements confirmed that the  $Ln:W$  atomic ratio was close to 1:1.5 in the as synthesized precursors in an agreement with the synthesis strategy. The residual concentration of sodium from reactants after careful washing did not exceed 0.07 wt.%. Thus, the as synthesized precursor powders corresponded to stoichiometry  $Ln_2(WO_4)_3 \cdot xH_2O$  and the potential formation of sodium-containing double tungstates  $NaLn(WO_4)_2$  can be decisively ruled out.

#### 3.2. STA Study

The freshly synthesized precursor powders were characterized using STA to address their thermal stability and determine characteristic temperatures of major structure formation trends therein. According to the TG data, the most significant mass loss ( $\sim 80\%$  of the total loss) is observed below  $\sim 200\text{--}220^\circ\text{C}$  (Figure 1a).

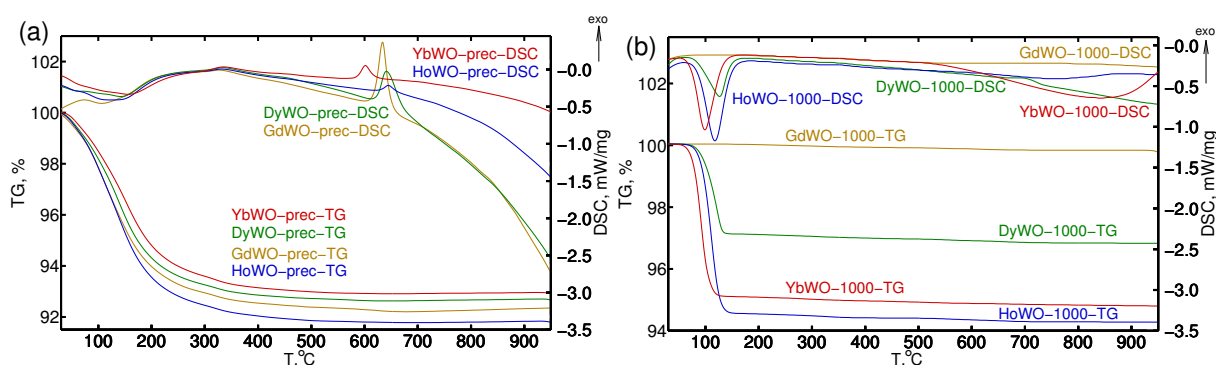


**Figure 1.** STA curves for  $Ln$  tungstates precursors  $LnWO\text{-}prec$  (a) and  $LnWO\text{-}1000\text{-}1.5y$  ( $Ln = Gd, Dy, Ho, Yb$ ) powders (b).

Some distinct sections are clearly seen in the TG curves, which are characterized by different slopes and thus to different mass loss rates ( $\Delta m/\Delta T$ ). The first section occurs in a range from  $50^\circ\text{C}$  and  $90\text{--}120^\circ\text{C}$  ( $\Delta m/\Delta T \sim 0.03\%/^\circ\text{C}$ ), whereas the second region lies in a range from  $90$  to  $120^\circ\text{C}$  to  $155\text{--}170^\circ\text{C}$  ( $\Delta m/\Delta T \sim 0.05\%/^\circ\text{C}$ ), and the third one—from  $155$  to  $170^\circ\text{C}$  up to  $200\text{--}220^\circ\text{C}$  ( $\Delta m/\Delta T \sim 0.02\%/^\circ\text{C}$ ). The corresponding DSC curves also reveal two weak broadened endothermic peaks at temperature around  $50\text{--}60^\circ\text{C}$  and  $140\text{--}150^\circ\text{C}$ , slightly varying for precursors bearing different  $Ln$  types. This clearly implies that the loss of water from precursors proceeds via two distinct stages, which in turn, assumes that the samples bear two types of non-structural occluded  $H_2O$ . A heating to higher temperature of  $550\text{--}600^\circ\text{C}$  removes the residual structural more strongly bonded water. This is in accord with earlier results reported elsewhere [41], claiming that the dehydration of  $Ln$  tungstates and molybdates is divided into several distinct stages: the adsorbed water gets desorbed at  $50\text{--}70^\circ\text{C}$ , the occluded water is removed—at  $50\text{--}150^\circ\text{C}$ , the hydration water is removed—at  $150\text{--}250^\circ\text{C}$ , and the water of OH-groups are finally removed at as high as  $500^\circ\text{C}$ . The total mass loss of the samples for the series of precursors under study lies in the range from  $7.14\%$  to  $8.23\%$  (Table 2). The nominal water content in each sample, which can be formulated as  $Ln_2(WO_4)_3 \cdot (4.7\text{--}5.5)H_2O$  (depending on the  $Ln$  type), is given in Table 2.

Upon a further increase in temperature to  $\sim 600^\circ\text{C}$  all precursors demonstrate a peak of exothermic processes in the DSC curves (Figure 1a, Table 2). The exact temperature corresponding to the peak maximum increases along the series from Gd to Ho but starts to decrease again on going to Yb ( $600.9^\circ\text{C}$ ). These exothermic processes correlated with the XRD data (see Section 3.3 below) and are due to the initiation of the crystallization of the precursor powders giving rise to  $Ln_2(WO_4)_3$ . It is of note that Gd and Dy tungstates are



characterized by higher crystallization enthalpies (116 J/g and 91 J/g, respectively) with respect to analogous Ho and Yb derivatives (17 J/g and 24 J/g, respectively) (Table 2).

**Table 2.** STA results of as-prepared lanthanoid tungstates precursors.

<i>Ln</i> Type	$T_{crystal}$ , °C	$\Delta H_{crystal}$ , J/g	$\Delta m$ , %	Composition
Gd	633.7	116	7.83	Gd <sub>2</sub> (WO <sub>4</sub> ) <sub>3</sub> ·5.0H <sub>2</sub> O
Dy	637.5 (650.8 shoulder)	91	7.43	Dy <sub>2</sub> (WO <sub>4</sub> ) <sub>3</sub> ·4.8H <sub>2</sub> O
Ho	643.8	17	8.23	Ho <sub>2</sub> (WO <sub>4</sub> ) <sub>3</sub> ·5.4H <sub>2</sub> O
Yb	600.9	24	7.14	Yb <sub>2</sub> (WO <sub>4</sub> ) <sub>3</sub> ·4.7H <sub>2</sub> O

Experimental STA curves for well-crystallized samples stored in air for 1.5 year coded as *Ln*WO-1000-1.5y (*Ln* = Gd, Dy, Ho, Yb) are shown in Figure 1b. As it can be seen from Figure 1b, the sample GdWO-1000-1.5y contains the minimum amount of absorbed water. Heavier *Ln* (*Ln* = Dy, Ho, Yb) tungstates demonstrate higher hydration degrees. Furthermore, their dominant mass loss (up to 90–95%) occurs in a temperature range of 60–180 °C. So that a hydration degree (*n*H<sub>2</sub>O) (i.e., the water amount per 1 mol *Ln*<sub>2</sub>(WO<sub>4</sub>)<sub>3</sub>) was calculated based on mass losses at 200 °C, observed from thermogravimetric curves, obtained under the same conditions described for STA of the precursors. The apparent effects of the lanthanoid cation type and duration of storage in air on the hydration degrees of the samples are given in Table S3.

As it can be judged from Table S3, the maximum content of absorbed water is observed for the Ho and Yb tungstates, and their stoichiometries thus nearly correspond to trihydrates. Our experimental values for the hydration degrees of these samples (Table S3) are somewhat larger than the ones previously reported [9,27]. This discrepancy could be due to the fact that the hydration degrees reported in [9,27] were calculated as mass losses in a temperature range between 60 °C and 120 °C and thus the dehydration could be incomplete in those cases. The Dy tungstate occupies an intermediate position between Gd and Ho, Yb derivatives.

We observe that *Ln* (*Ln* = Dy, Ho, Yb) tungstates exposed to air for one day contained lower amounts of absorbed water with respect to their analogues experienced longer air storage durations from 7 to 9 days to 1.5 year. Moreover, air aging resulted in an apparent shift in the dehydration temperature towards higher values, which could indirectly indicate progressive conversion of weakly bound occluded water molecules to hydration water incorporated into the crystal structure of initially unhydrated rare-earth tungstates. This observation is in full accord with ab initio calculation results [42], which predict that the O end of the inserted H<sub>2</sub>O molecules prefer to bind to *Ln*<sup>3+</sup> or W<sup>6+</sup> cations, whereas the two H atoms of each H<sub>2</sub>O molecule tend to point outward to the nearby bridge O atoms shared by *Ln*O<sub>6</sub> octahedra and WO<sub>4</sub> tetrahedra, and form hydrogen bonds, which play a key role in the binding between H<sub>2</sub>O and the materials.

The observation of Ho and Yb tungstates trihydrates in samples exposed to air for few days indicate that the water absorption proceeds relatively fast. To learn more details, we studied kinetics of the hydration. According to results obtained, fresh non-hydrated *Ln*WO-1000 (*Ln* = Dy, Ho, Yb) powders accumulate 80–85% of hydration theoretical maximum upon exposure to air within 1–1.5 h (Figure 2a). This is in a good agreement with the literature data [43]. They reported that water absorption by (Lu<sub>0.6</sub>Eu<sub>0.4</sub>)<sub>2</sub>(WO<sub>4</sub>)<sub>3</sub> tungstate is completed for 3–4 h. As it can be seen from Figure 2a, Dy<sub>2</sub>(WO<sub>4</sub>)<sub>3</sub>-1000 °C is characterized by the maximum water absorption rate. The resultant descending order of hydration rates looks as follows: Dy<sup>3+</sup> (0.912 Å; CN = 6) → Ho<sup>3+</sup> (0.901 Å; CN = 6) → Yb<sup>3+</sup> (0.868 Å; CN = 6). This regularity can be rationalized by a balance of kinetics- and energy-related factors. The absolute value of water absorption energy in *Ln* tungstates, according to [42], is expected to decrease as the ionic radius of the *Ln*<sup>3+</sup> cation decreases.

It is of note that DyWO-1000 powders demonstrated the most peculiar behavior among the series under study. Two samples quenched in air (DyWO-1000-1.5y) and in a

desiccator (DyWO-1000-desic-1.5y) revealed significantly different hydration degrees after prolonged storage in air for 1.5 year (Table S3, Figure 2b). Furthermore, both powders lost their hygroscopicity after repeated heating to 1000 °C (DyWO-1000-repeat-1.5y). This is in contrast with the behavior of Ho and Yb tungstates, which retained their hygroscopicity by quickly absorbing water after repeated heating (Table S3). The DSC curve of DyWO-1000-1.5y sample quenched in air and then stored for 1.5 year reveals an exothermic peak at 700 °C. However, similar peak is observed neither for the Dy<sub>2</sub>(WO<sub>4</sub>)<sub>3</sub>-1000 °C sample cooled in a desiccator (DyWO-1000-desic-1.5y) nor for the sample after a repeated heating up to 1000 °C (DyWO-1000-repeat-1.5y).

These features of the thermal behavior related to the hydration degrees in *Ln* tungstates under study are evidently determined by differences in their crystal structures, which is discussed in more detail below in Section 3.3.

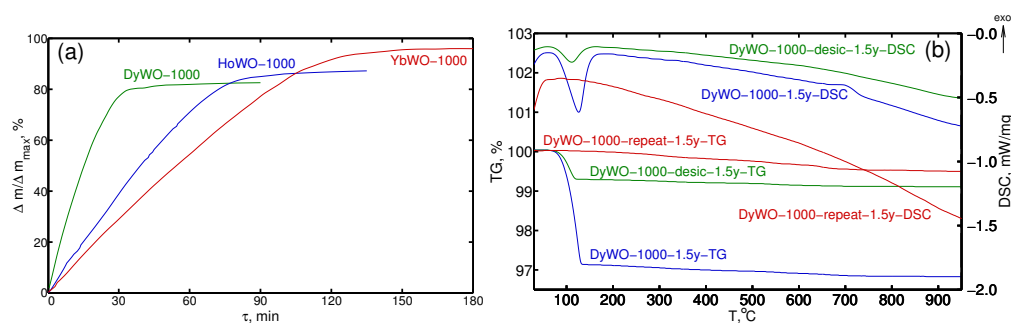


**Figure 2.** Hydration kinetics for *Ln*WO-1000 (a) and STA curves for differently treated Dy tungstate samples (b): (1) DyWO-1000-1.5y; (2) DyWO-1000-desic-1.5y; (3) DyWO-1000-repeat-1.5y.

### 3.3. XRD Study

The as prepared precursors were essentially X-ray amorphous for all  $Ln^{3+}$  cations. Their experimental diffraction patterns revealed however a broad but distinct peak indicative of the emergence of specific short-range order therein. The huge width of the diffraction peak for the precursors prevented us from an accurate evaluation of crystallite sizes by the Scherrer formula. We thus believe that the crystallite sizes for these samples do not exceed ~1 nm. The precursor crystallization process started at ~600 °C (Figure 3a). As it can be easily followed by Figure 3a, GdWO-600-6d and DyWO-600-6d powders were characterized by identical monoclinic structures (sp. gr.  $C12/c1(15)$ ). Meanwhile, a residual amorphous halo was apparent in patterns of DyWO-600-6d and HoWO-600-6d, which is indicative of the partial preservation of amorphous fraction. The maximum residual amorphous phase fraction was observed for HoWO-600-6d. For the heavier Yb tungstate YbWO-600-6d, however, only very low amorphous fraction was observed. Furthermore, this powder can be regarded as nanocrystalline with an effective crystallite size of 26(1) nm characterized by an alternative monoclinic structure (sp. gr.  $P12_1/a1(14)$ ). Crystallization trends observed by X-ray diffraction are in accord with crystallization temperatures estimated from DSC curves measured for precursors (see Figure 1a, Table 2).

Calcination of the samples at a higher temperature of 1000 °C gave rise to further increase in the crystallite size (narrowing of the diffraction peaks). Moreover, the phase composition of the samples also changed (Figure 3b–d). According to our analysis, the exact phase composition of a sample depends strongly both on the type of the lanthanoid cation therein and its thermal history (Table S4).

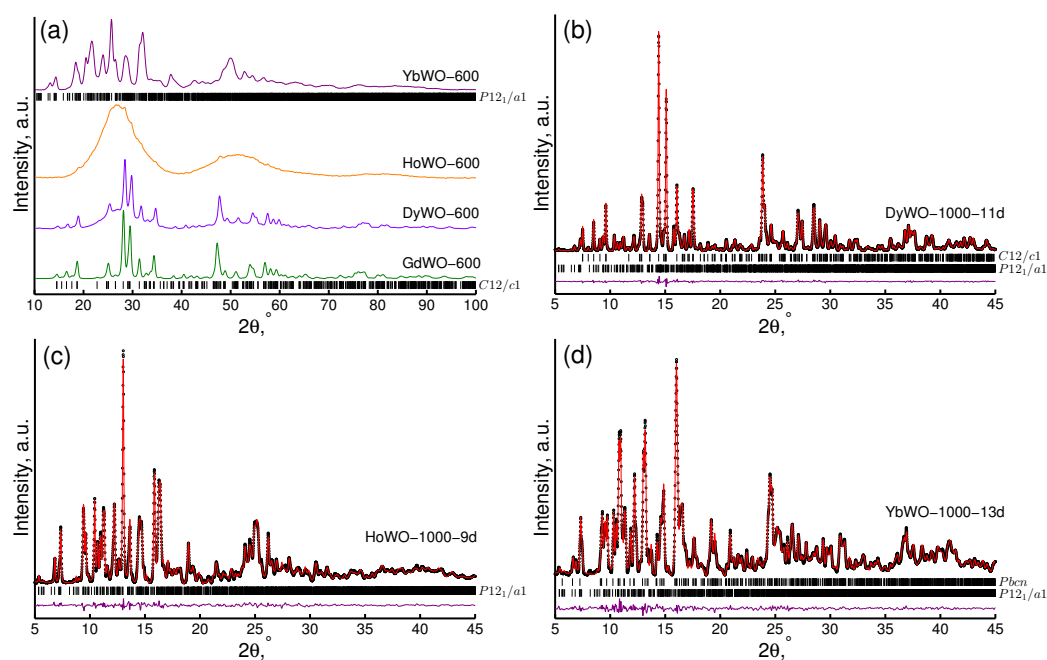


**Figure 3.** XRD patterns of  $LnWO$ -600-6d ( $Cu\ K\alpha$ ) (a) and s-XRD patterns ( $\lambda = 0.8\ \text{\AA}$ ) of  $DyWO$ -1000-11d (b),  $HoWO$ -1000-9d (c),  $YbWO$ -1000-13d (d).

All hydrated heavy  $Ln$  tungstates ( $Ln = Dy, Ho, Yb$ ) powders are characterized by the monoclinic structure (sp. gr.  $P12_1/a1(14)$ ) similar to that identified and studied in detail for  $In_2(WO_4)_3$  [44]. However, this conclusion contradicts to other literature data claiming that trihydrated form of heavy  $Ln$  tungstates  $Ln_2(WO_4)_3 \cdot 3H_2O$  has either orthorhombic [9] or monoclinic structure (sp. gr.  $P2/m$ ) [8,22,23]. It is worth noting that the cell parameters we obtained (Table S4) agree well with data reported by other authors [8,23].

As it can be seen from Table S4, the annealing of precursors at  $1000\ ^\circ C$  gives rise to the formation of single-phase samples for  $Gd_2(WO_4)_3$  and  $Ho_2(WO_4)_3$ , but two-phase mixtures are afforded for  $Dy_2(WO_4)_3$  and  $Yb_2(WO_4)_3$ .

In the case of  $Gd_2(WO_4)_3$ , both the freshly prepared sample and the one after a prolonged storage in air (1.5 year) contain only the monoclinic structure (sp. gr.  $C12/c1$ ) with only minute modifications related to the air storage expressed as a some decrease in the apparent crystallite size. The best-fit atomic coordinates and isothermal temperature factors for the monoclinic structure (sp. gr.  $C12/c1$ ) of well-crystallized  $Gd_2(WO_4)_3$  and  $Dy_2(WO_4)_3$  prepared by calcination at  $1000\ ^\circ C$  from Rietveld refinements were reported by us earlier [32]. A sketch of the monoclinic crystal structure (sp. gr.  $C12/c1$ ) in a polyhedral representation is shown in Figure 4a. This crystal structure type is dominant for light lanthanoid tungstates [12–18].

A complex evolution of crystal structures was observed for the two-phase samples.  $Dy_2(WO_4)_3$  can be regarded as a boundary compounds demonstrating the  $C12/c1(15) \rightarrow P12_1/a1(14)$  phase transition (Figure S1). As it can be seen from Table S4, the fraction of the monoclinic structure (sp. gr.  $P12_1/a1(14)$ ) increases in the course of the air storage. Furthermore, the sample  $DyWO$ -1000-1.5y prepared by quenching in air contained the monoclinic phase (sp. gr.  $P12_1/a1(14)$ ) in an amount several fold higher than that in the  $DyWO$ -1000-desic-1.5y sample quenched in a desiccator, despite identically long post-synthesis exposure to air.

The repeated annealing of both samples to  $1000\ ^\circ C$  gave rise to single-phase powders with the monoclinic structure (sp. gr.  $C12/c1(15)$ ), i.e., initiated the  $P12_1/a1(14) \rightarrow C12/c1(15)$  phase transition (Table S4). Therefore, we may associate the exothermic DSC peak around  $700\ ^\circ C$  for the sample  $DyWO$ -1000-1.5y with the  $P12_1/a1(14) \rightarrow C12/c1(15)$  phase transition (Figure 2b). A combined analysis of X-ray diffraction (Table S4) and STA



results (Table S3) indicates that it is the monoclinic structure (sp. gr.  $P12_1/a1(14)$ ) that is exclusively responsible for the intrinsic hygroscopicity of the heavy lanthanoid tungstates. The apparent hydration degree for DyWO-1000-1.5y corrected for the experimental fraction of the  $P12_1/a1$  phase is 3.4, which is reasonably close to respective values in Ho and Yb tungstate trihydrates (Table S3).

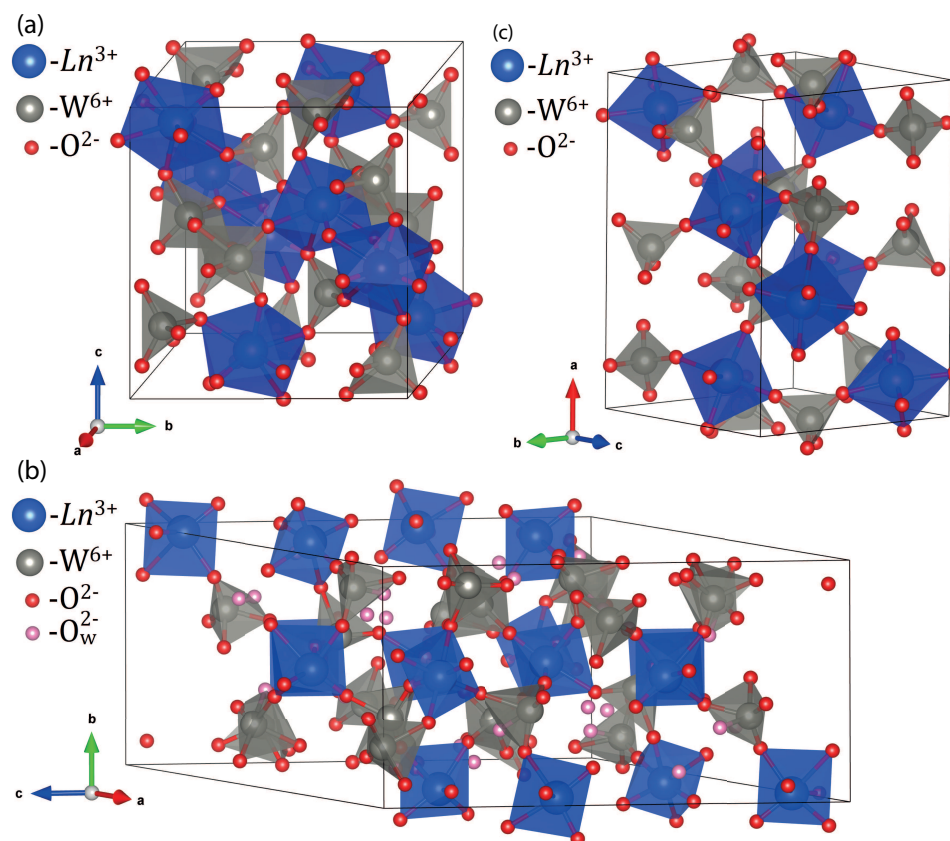


**Figure 4.** (a) Polyhedral representation of the monoclinic structure (sp. gr.  $C12/c1$ ) encountered as the main phase in lanthanoid tungstates  $Ln_2(WO_4)_3$  ( $Ln = Gd, Dy$ ). The lanthanoid  $Ln^{3+}$  cations are eight-fold coordinated (shown in blue). The  $W^{6+}$  cations form  $WO_4$  tetrahedra (shown in grey). All the oxide  $O^{2-}$  anions are shown in red; (b) Polyhedral representation of the monoclinic structure (sp. gr.  $P12_1/a1$ ) encountered as the main phase in lanthanoid tungstates  $Ln_2(WO_4)_3$  ( $Ln = Ho, Yb$ ). The lanthanoid  $Ln^{3+}$  cations are six-fold coordinated (shown in blue). The  $W^{6+}$  cations form  $WO_4$  tetrahedra (shown in grey). All the oxide  $O^{2-}$  anions are shown in red. Additional oxygen atoms of hydration  $H_2O$  molecules are shown in pink; (c) Polyhedral representation of the orthorhombic structure (sp. gr.  $Pbcn$ ) encountered as an admixture phase in  $Yb_2(WO_4)_3$ . The  $Yb^{3+}$  cations are six-fold coordinated (shown in blue). The  $W^{6+}$  cations form  $WO_4$  tetrahedra (shown in grey). The oxide  $O^{2-}$  anions are shown in red.

The  $Ho_2(WO_4)_3$  samples contain predominantly the monoclinic phase (sp. gr.  $P12_1/a1$ ) corresponding to a hydrated holmium tungstate with approximately 3.0–3.5 hydration water molecules per formula unit. This was not altered to any significant extent by a prolonged storage in air (1.5 year). Though the storage resulted in a small decrease both in cell parameters and volume as well as in an apparent decrease in a crystallite size. Both quenching in air and in a desiccator afforded samples with the same phase compositions. The quenching, having no effect on the phase composition, led to some decrease in the cell parameters, its volume, and the crystallite size (Table S4).

We tried to refine the atomic coordinates in the monoclinic phase (sp. gr.  $P12_1/a1$ ) of holmium tungstate using crystallographic parameters for anhydrous  $In_2(WO_4)_3$  [44]. Positions of the cations were allowed to vary with identical thermal parameters. Positions of the oxygen atoms were refined with geometrical constraints to yield reasonable Ho-O and

W-O bond lengths. At last stages of the refinement, six extra oxygen atoms per asymmetric unit corresponding to hydration water molecules were placed into voids of the crystal structure. The list of best-fit coordinates is given in Table S5. Polyhedral representation of the monoclinic structure (sp. gr.  $P12_1/a1$ ) encountered as the main phase in  $\text{Ho}_2(\text{WO}_4)_3$  is shown in Figure 4b.

In the case of Yb, a two-phase sample YbWO-1000-13d was afforded simultaneously containing monoclinic (sp. gr.  $P12_1/a1(14)$ ) tungstate trihydrate and an orthorhombic phase (sp. gr.  $Pbcn(60)$ ) typical for the unhydrated form of heavy *Ln* tungstates (Table S4). As it can be seen from Table S4, the fraction of the monoclinic structure (sp. gr.  $P12_1/a1(14)$ ) increases in the course of air storage, which ultimately results in a complete disappearance of the orthorhombic phase (sp. gr.  $Pbcn(60)$ ) (Figure S2). Powders quenched in air and in a desiccator and then aged in air were characterized by similar phase compositions and cell parameters (Table S4). Polyhedral representation of the orthorhombic structure (sp. gr.  $Pbcn$ ) encountered as an admixture phase in  $\text{Yb}_2(\text{WO}_4)_3$  is shown in Figure 4c.

The powder diffraction results can be thus summarized as follows. Within the same crystal structure type (the same syngony and space group) unit cell parameters and volume regularly decrease with a nominal decrease in the  $\text{Ln}^{3+}$  cation radius. For the two-phase samples, the fraction of the monoclinic phase (sp. gr.  $P12_1/a1(14)$ ) increases as air exposure duration increases. At that the unit cell parameters and volume also tend to decrease. The decrease in the unit cell volume upon progressive hydration corresponds to earlier reported data [45]. Additionally, the aging is accompanied by a decrease in the apparent crystallite size (Table S4).

It is important to note that both orthorhombic structure (sp. gr.  $Pbcn$ ) and monoclinic structure (sp. gr.  $P12_1/a1$ ) are less dense as compared to the monoclinic structure (sp. gr.  $C12/c1$ ) and contains some structural voids accessible for water molecules, which can be considered as a driving force of the hydration (see above Section 3.2 and below Section 3.5.2). The two former structures are closely related to each other. The monoclinic structure (sp. gr.  $P12_1/a1$ ) can be regarded as a lower-symmetry superstructure of the parent orthorhombic structure (sp. gr.  $Pbcn$ ) resulted from a loss of one two-fold symmetry axis. We speculate that the orthorhombic phase is observed for heavier lanthanoid tungstates at an intermediate stage of hydration, whereas the full hydration stabilizes the monoclinic structure (sp. gr.  $P12_1/a1$ ).

### 3.4. X-ray Absorption Spectroscopy

The crystal structure as imaged by diffraction corresponds to an ensemble-averaged atomic configurations. Furthermore, the local structure probed by other techniques could differ drastically from the crystallographic data. We used local structure-sensitive X-ray absorption fine structure (XAFS) spectroscopy to elucidate the local atomic environment of W and *Ln* atoms within the *Ln* tungstates under study and compare them with diffraction-extracted crystallographic parameters.

#### 3.4.1. W $L_1$ - and $L_3$ -Edges XAFS Study

The analysis of XAFS spectra at the W  $L_1$ - and  $L_3$ -edges is commonly applied to gather information on the local environment symmetry, coordination polyhedra, and oxidation state of the W species in various complex oxide compounds due to unique properties of this technique [24,25].

#### W $L_1$ -Edge XANES

Figure 5a shows the W  $L_1$ -edge XANES spectra of hydrated well-crystallized *Ln* tungstate powders. All the spectra manifest a main-edge (the dipole-allowed  $2s \rightarrow 6p$  electron transitions) and a sharp pre-edge peak (the dipole forbidden  $2s \rightarrow 5d$  electron transitions) gathering a non-zero intensity due to the  $p-d$  hybridization [24]. The exact position (12,102 eV) and intensity of the pre-edge peak reveal no statistically significant dependence on the *Ln* type. They are also similar to those in  $\text{Na}_2\text{WO}_4 \cdot 2\text{H}_2\text{O}$  (the experi-

mental position is 12,103 eV), which is a reference sample with tetrahedral  $\text{WO}_4$  units [24]. This indicates the presence of undisturbed tetrahedral configurations  $\text{WO}_4$  in the studied  $\text{Ln}$  tungstates regardless of the  $\text{Ln}$ , i.e., their crystal structure type (see Table S4). As the  $\text{Ln}$  atomic number increases, the position of the main absorption maximum in the W  $L_1$ -edge spectra shifts towards higher energies (from 12,131.9 eV for  $\text{Gd}_2(\text{WO}_4)_3$  to 12,135.9 eV for  $\text{Yb}_2(\text{WO}_4)_3$ ) (Figure 5a), which could be due to a shift in the exact position of the Fermi level for heavy  $\text{Ln}$  tungstates due to an increase in the number of  $5d$  electrons localized in hybridized  $p-d$  orbitals.

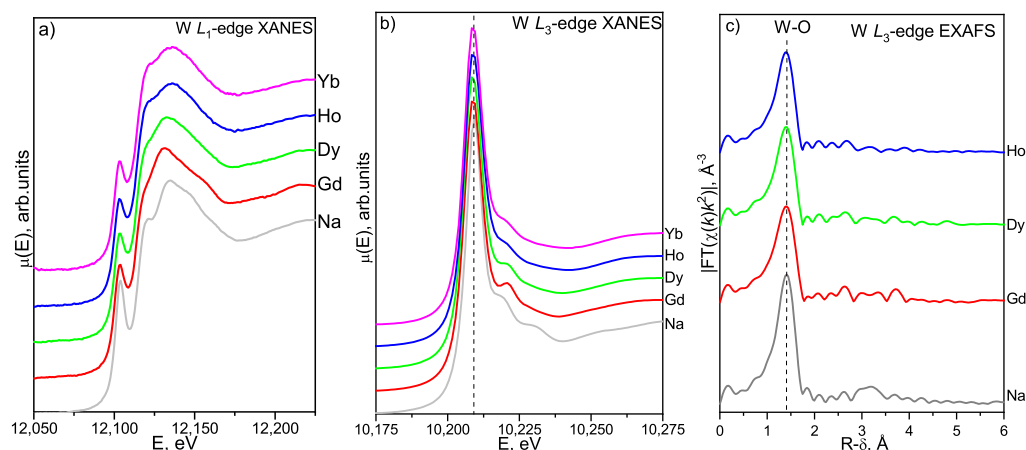


**Figure 5.** W  $L_1$ -(a) and  $L_3$ -edge (b) XANES spectra and W  $L_3$ -edge EXAFS FT moduli (c) of hydrated  $\text{LnWO-1000-1.5y}$  powders and  $\text{Na}_2\text{WO}_4 \cdot 2\text{H}_2\text{O}$  (reference sample).

#### W $L_3$ -Edge XANES

Figure 5b displays the W  $L_3$ -edge XANES spectra of hydrated well-crystallized  $\text{Ln}$  tungstate powders along with reference sample  $\text{Na}_2\text{WO}_4 \cdot 2\text{H}_2\text{O}$ . As it becomes evident from Figure 5b, the near-edge spectra reveal a common well-resolved narrow and intense asymmetric peak due to the dipole-allowed electron transitions  $2p_{3/2} \rightarrow 5d$ . The spectral parameters of the white line peak for all  $\text{Ln}_2(\text{WO}_4)_3$  samples under study are virtually identical to each other for all the  $\text{Ln}$  types in the study and are again close to those in the  $\text{Na}_2\text{WO}_4 \cdot 2\text{H}_2\text{O}$  reference (10,209 eV). This confirms the earlier suggestion that undisturbed  $\text{WO}_4$  tetrahedra predominate as major structural units in all studied  $\text{Ln}_2(\text{WO}_4)_3$  samples, irrespective of their crystal structure type (see Table S4). An evident weakening of the right-hand shoulder of the white line (at about 10,218 eV) for heavier lanthanoids (that is well pronounced on going from the spectrum of gadolinium compound to that of dysprosium) can be due to a change in the effective coordination geometry of the  $\text{WO}_4$  tetrahedral units accompanying the transformation of the  $\text{Ln}_2(\text{WO}_4)_3$  structure type from one monoclinic (sp. gr.  $\text{C12}/c1(15)$ ) in  $\text{Gd}_2(\text{WO}_4)_3$  to another monoclinic phase (sp. gr.  $\text{P12}_1/a1(14)$ ) in heavier tungstates  $\text{Ln}_2(\text{WO}_4)_3$  ( $\text{Ln} = \text{Dy}, \text{Ho}, \text{Yb}$ ).

#### W $L_3$ -Edge EXAFS

The Fourier transform moduli of W  $L_3$ -edge EXAFS spectra for hydrated well-crystallized  $\text{LnWO-1000-1.5y}$  samples are shown in Figures 5c and S3. The W  $L_3$ -edge EXAFS FT moduli are dominated by a single intense peak at 1.4 Å, assigned to the W-O coordination shell (CS) formed by  $\text{WO}_4$  tetrahedra. Longer-distance CSs are characterized by negligible intensities. This assumes that the short-range atomic order of heavy metal ions around the W site is rather irregular in the studied  $\text{LnWO-1000-1.5y}$  samples. Positions of FT modulus peaks shown in Figure 5c are apparently shorter than real interatomic distances due to the phase shift associated with the photoelectron backscattering. Real bond lengths obtained from EXAFS non-linear curve-fitting are given in Table 3.

**Table 3.** W  $L_3$ -edge EXAFS best-fit results for the W-O coordination shells for hydrated well-crystallized  $LnWO_4 \cdot 1000-1.5y$  ( $Ln = Gd, Dy, Ho, Yb$ ) powders.

Lanthanoid Cation	Model 1/2	N	R, Å	$\sigma^2$ , Å <sup>2</sup>	R <sub>dis</sub> , %
Gd	1	3.7(5)	1.79(1)	0.004(1)	8
		1.2(5)	2.19(1)	0.007(1)	
	2	2 (fixed)	1.76(1)	0.008(1)	8
		2 (fixed)	1.80(1)	0.002(1)	
		1 (fixed)	2.17(1)	0.002(1)	
Dy	1	3.5(5)	1.79(1)	0.003(1)	9
		1.2(5)	2.18(1)	0.008(1)	
	2	2 (fixed)	1.76(1)	0.010(1)	9
		2 (fixed)	1.79(1)	0.002(1)	
		1 (fixed)	2.16(1)	0.003(1)	
Ho	1	3.6(5)	1.78(1)	0.003(1)	12
		0.8(5)	2.13(1)	0.003(1)	
	2	2 (fixed)	1.74(2)	0.002(2)	12
		2 (fixed)	1.82(1)	0.002(1)	
		1 (fixed)	2.11(1)	0.004(1)	
Yb	W L <sub>3</sub> - and Yb L <sub>1</sub> -edge spectra strongly overlap				

Values given in parentheses correspond to the estimated standard deviations (esd); N is the coordination number; R is the interatomic distance;  $\sigma^2$  is the Debye–Waller factor (DWF);  $R_{dis}$  is the discrepancy index.

We applied two structural models to approximate the first W-O CS peak in EXAFS FTs. According to preliminary evaluations, we established that a set of a few W-O distances is required to achieve a reasonable fit, i.e., the W-O CS is split. The best-fit values of the local-structure parameters are compiled in Table 3. Despite W-O distance of 1.75–1.8 Å typical of tetrahedrally coordinated tungsten, an extra component corresponding to a W-O distance of 2.1–2.2 Å was necessary to reproduce the experimental curve. Furthermore, we performed the curve fitting with refinable coordination numbers (model 1) and coordination numbers fixed at idealized values “2+2+1” (model 2). The results obtained clearly indicate that the  $WO_4^{2-}$  tetrahedra in the heavy lanthanoid tungstates are actually noticeably distorted. Unfortunately, due to the partial overlap of W  $L_3$ -edge and Yb  $L_1$ -edge spectra, the accuracy of local-structure parameters did not allow us to establish a reliable dependence of the W-O bond lengths on the lanthanoid cation type, although the trend of bond length shortening towards the end of the rare-earth series is evident.

### 3.4.2. Lanthanoid $L_3$ -Edge XAFS Study

#### $Ln$ $L_3$ -Edge XANES

The  $Ln$   $L_3$ -edge XANES spectra of hydrated well-crystallized  $LnWO_4 \cdot 1000-1.5y$  samples are shown in Figure 6a. The narrow strong main-edge peaks at +2.5 eV of the  $E - E_0$  scale (FWHM is approximately 6 eV) are due to the  $Ln 2p_{3/2} \rightarrow 5d$  electronic transitions [46]; their positions and shapes lie within normal values typically observed for compounds containing trivalent lanthanoid ions. The principal spectral parameters in the  $Ln$   $L_3$ -edge spectra demonstrate prominent similarity along the lanthanoid series, which strongly assumes trivalent  $Ln^{3+}$  cations are exclusively present in the analyzed compounds. In the  $Ln$   $L_3$ -edge XANES spectral of Dy, Ho, and Yb tungstates, the white line is followed by a plateau. Taking into account the s-XRD results discussed above (Table S4), we may associate this plateau with a change in the local symmetry of  $Ln$  atoms due to the transformation of one monoclinic structure  $C12/c1(15)$  into another one  $P12_1/a1(14)$ .

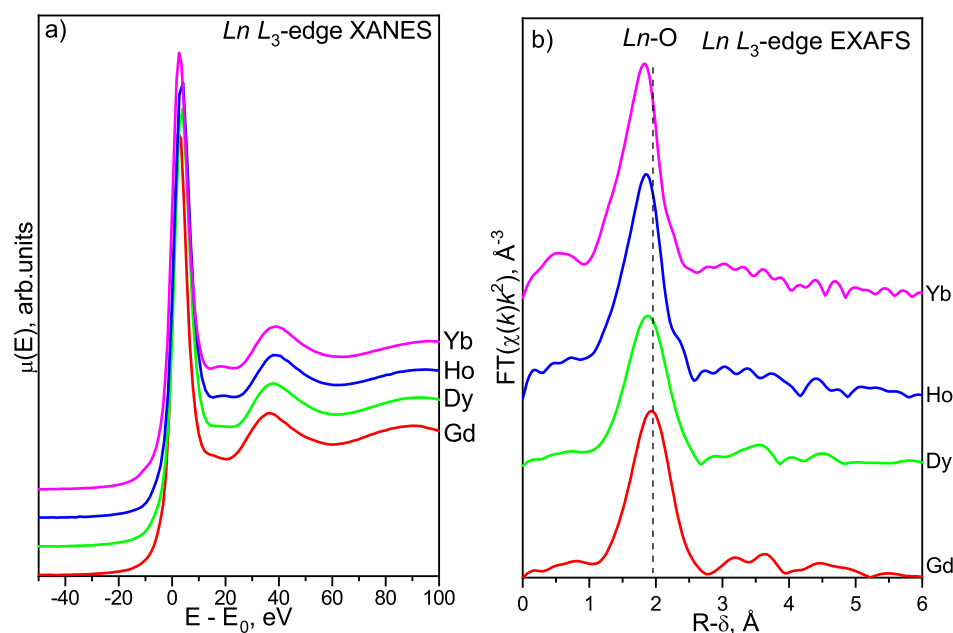


**Figure 6.**  $Ln$   $L_3$ -edge XANES spectra (a) and EXAFS FT moduli (b) of hydrated  $LnWO$ -1000-1.5y.

#### $Ln$ $L_3$ -Edge EXAFS

The FT moduli of  $Ln$   $L_3$ -edge EXAFS-spectra of hydrated well-crystallized  $LnWO$ -1000-1.5y samples are displayed in Figures 6b and S4. In all experimental curves, the first dominant peak appears around 1.8–1.9 Å; it can be assigned to the  $Ln$ -O CS. Other coordination shells are weak and smeared (similar to the case of W  $L_3$ -edge EXAFS FTs). This indicates a significant degree of local disorder around the  $Ln^{3+}$  cations in  $Ln_2(WO_4)_3$ . As it becomes clear from Figure 6b, the positions of lanthanoid-oxygen  $Ln$ -O and lanthanoid-metal  $Ln$ -M components move to shorter interatomic distances as the  $Ln^{3+}$  cation radii decrease (or, equivalently, as the  $Ln$  atomic numbers increase).

Similarly to the case of the aforementioned W-O CS coordination shell, we started with a simple local-structure model with  $Ln$ -O interatomic distances  $R$ , corresponding Debye-Waller factors  $\sigma^2$ , and coordination numbers  $N$  were allowed to refine freely to achieve a best fit. According to fits in this simplest model with one  $Ln$ -O shell (Table 4, model 1), the effective  $Ln$ -O bond length shortens for  $Ln^{3+}$  cations with nominally smaller ionic radii along the series Gd–Dy–Ho–Yb. As it can be seen from Table 4, the best-fit coordination numbers  $N$  are close to 8 for the Gd and Dy tungstates that possess the monoclinic structure (sp. gr.  $C12/c1(15)$ ). A switch of the structure type to another monoclinic lattice (sp. gr.  $P12_1/a1(14)$ ) in  $Ho_2(WO_4)_3$  is accompanied by a decrease in the effective coordination number. The trend continues for Yb tungstate, in which  $N$  approaches a value of 6, which is typical for the structure of heavy lanthanoid tungstates described in the literature [9,23,41]. Our analysis indicated that the change in the effective  $N$  upon the  $C12/c1(15) \rightarrow P12_1/a1(14)$  transformation is continuous rather than abrupt.

A further analysis was carried out using a more complicated local structure model based on fixed values of  $N$ . The model postulated the  $Ln$ -O coordination shell split into two components with fixed coordination numbers of  $N_1 = 6$  and  $N_2 = 2$  (Table 4, model 2). The validity of this model was evaluated using the Fisher's test [39]. As it can be seen from Table 4, the statistical probability of this model with the split  $Ln$ -O coordination shell ( $6 + 2$ ) is 23% for  $Gd_2(WO_4)_3$ . This criterion increases to 52.7% for  $Dy_2(WO_4)_3$ , when an alternative monoclinic structure (sp. gr.  $P12_1/a1(14)$ ) emerges according to X-ray diffraction data. In the case of  $Ho_2(WO_4)_3$ , which contains strictly single-phase (sp. gr.  $P12_1/a1(14)$ ), the model becomes statistically reliable with the Fisher's criterion as high as 98%. For  $Yb_2(WO_4)_3$  with the even smaller ionic radius of the lanthanoid cation  $Yb^{3+}$ , the basic local-structure model assumes that the  $Ln$ -O coordination shell is formed by one unsplit component



with the coordination number of 6. In the full agreement with intuitive anticipation, the effective  $Ln$ -O bond lengths refined from EXAFS spectra (Table 4) decrease along the series Gd-Dy-Ho-Yb of descending ionic radii. It is also of note that the spread between the two components within a split shell increases as the  $Ln^{3+}$  cation radius decreases in the series Gd (1.053 Å) > Dy (1.027 Å) > Ho (1.015 Å), where it applies.

**Table 4.**  $Ln$   $L_3$ -edge EXAFS best-fit results for  $Ln$ -O shells of hydrated well-crystallized  $LnWO_4 \cdot 1000$ -1.5y powders ( $Ln$  = Gd, Dy, Ho, Yb).

Lanthanoid Cation	Model 1/2	N	R, Å	$\sigma^2$ , Å <sup>2</sup>	P, %	$R_{dis}$ , %
Gd	1	8.0(9)	2.39(2)	0.009(1)	-	8
	2	6 (fixed)	2.38(1)	0.009(1)	23	8
		2 (fixed)	2.40(1)	0.009(1)		
Dy	1	7.9(9)	2.34(2)	0.011(1)	-	8
	2	6 (fixed)	2.31(1)	0.008(1)	58	9
		2 (fixed)	2.44(1)	0.005(1)		
Ho	1	7.3(9)	2.32(2)	0.011(1)	-	11
	2	6 (fixed)	2.30(1)	0.008(1)	98	12
		2 (fixed)	2.45(2)	0.004(1)		
Yb	1	6.6(9)	2.22(1)	0.009(1)	-	12
	2	6 (fixed)	2.26(1)	0.007(1)	5	15
		-	-	-		

Values given in parentheses correspond to the estimated standard deviations (esd); N is the coordination number; R is the interatomic distance;  $\sigma^2$  is the Debye-Waller factor (DWF); P is the probability of the preferred choice of the model with two components;  $R_{dis}$  is the discrepancy index.

Therefore, based on a combined analysis of s-XRD and XAFS spectroscopy results, we envisage the following mechanism of the structural rearrangement at local level associated with the monoclinic lattice transformations  $C12/c1(15) \rightarrow P12_1/a1(14)$ . The onset of the transformation falls onto  $Gd_2(WO_4)_3$  (Tables S4 and 4). The Gd-O coordination shell at the local level tends to split into two component (6 + 2) at the dominance of the monoclinic structure (sp. gr.  $C12/c1(15)$ ). With a further decrease in the  $Ln^{3+}$  cation radius the statistical significance of the  $Ln$ -O CS splitting as well as of the distance spread between the components increases, which is accompanied by the appearance of the monoclinic structure (sp. gr.  $P12_1/a1(14)$ ) in  $Dy_2(WO_4)_3$ , which further becomes the dominant phase in  $Ho_2(WO_4)_3$ . A further decrease in the  $Ln^{3+}$  radius stabilizes the monoclinic structure of hydrated  $Yb_2(WO_4)_3$  (sp. gr.  $P12_1/a1(14)$ ) with an unsplit Yb-O coordination shell with the coordination number of 6.

### 3.5. Vibrational Spectroscopy

Essential information concerning structural features of the sublattice formed by light oxygen atoms in the title heavy lanthanoid tungstates can be learned from vibrational spectroscopy, comprised of infrared absorption (IR) and Raman scattering spectroscopy. For nearly ideal tetrahedral  $WO_4$  moieties, 4 distinct normal vibrations are symmetrically allowed: stretching symmetric W-O ( $A_1$ ) bond vibration  $\nu_1$ , stretching bending W-O ( $E$ ) bond vibration  $\nu_2$ , stretching asymmetric ( $F_2$ ) and bending asymmetric ( $F_2$ ) W-O bond vibrations  $\nu_3$  and  $\nu_4$ , respectively, [43].

#### 3.5.1. Raman Study

Figure 7a demonstrates the experimental Raman spectra of  $Gd_2(WO_4)_3$  sample prepared by thermal treatments of the respective precursor powders at different temperatures. The Raman spectra of amorphous samples, i.e., the freshly prepared precursor and the

sample annealed at a low temperature of 500–550 °C, contain three broad vibrational bands around  $\sim 345\text{ cm}^{-1}$ ,  $825\text{ cm}^{-1}$ , and  $950\text{ cm}^{-1}$ , which are assigned to bending modes, and stretching modes of the  $\text{WO}_x$  moieties. The start of crystalline phase formation in the initially amorphous structure in  $\text{GdWO}_3$  yields the emergence of many new Raman bands (Figure 7a) corresponding to monoclinic structure of  $\text{Ln}$  tungstates [47]. A calcination at even higher temperature from 700 °C to 1000 °C induces no significant changes in the Raman spectra. This implies the oxygen sublattice formation in  $\text{Gd}_2(\text{WO}_4)_3$  is virtually complete at  $\sim 700\text{ °C}$ .

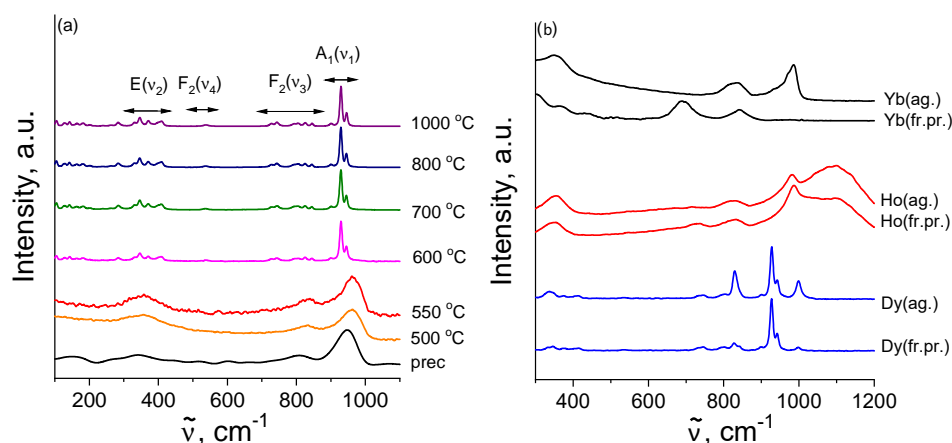


**Figure 7.** Raman spectra of  $\text{Gd}_2(\text{WO}_4)_3$  samples synthesized by the annealing of the precursor at different temperatures (a); fresh prepared and cooled in a desiccator (fr.pr.) and hydrated  $\text{Dy}_2(\text{WO}_4)_3$ ,  $\text{Ho}_2(\text{WO}_4)_3$  and  $\text{Yb}_2(\text{WO}_4)_3$  well-crystallized powders aged in air 1.5 years (ag.) (b).

The internal (above  $300\text{ cm}^{-1}$ ) vibrational bands observed in the spectrum of  $\text{Gd}_2(\text{WO}_4)_3$  ( $T_d$  point group symmetry) correspond to two slightly different  $\text{WO}_4$  tetrahedral units occurred in the unit cell. More specifically,  $\text{W}(1)\text{O}_4$  units ( $C_2$  site symmetry, mildly distorted tetrahedral units) and  $\text{W}(2)\text{O}_4$  units ( $C_1$  site symmetry, highly distorted tetrahedral units), which is in accordance with the earlier results for the monoclinic  $\text{La}_2(\text{WO}_4)_3$  phase reported in [48].

The appearance of an additional monoclinic phase (sp. gr.  $P12_1/a1(14)$ ) in  $\text{Dy}_2(\text{WO}_4)_3$  results in changing the shape of the Raman spectra (Figure 7b). The changes become cardinal upon a complete phase transition  $C12/c1(15) \rightarrow P12_1/a1(14)$  in  $\text{Ho}_2(\text{WO}_4)_3$  and  $\text{Yb}_2(\text{WO}_4)_3$ . Indeed, new Raman bands show up in the regions of  $340\text{--}350\text{ cm}^{-1}$ ,  $830\text{--}845\text{ cm}^{-1}$ , and  $985\text{--}1000\text{ cm}^{-1}$  (for  $\text{Ho}_2(\text{WO}_4)_3$  also in the region of  $1100\text{ cm}^{-1}$ ), and the modes at  $929\text{ cm}^{-1}$  and  $948\text{ cm}^{-1}$  completely disappear (Figure 7b). As can be seen from Figure 7b, the intensity of the Raman modes increased in the region of high wavenumbers ( $\sim 980\text{--}1100\text{ cm}^{-1}$ ) for all hygroscopic tungstates after storage in air compared to freshly obtained samples. This effect can be explained as follows. According to [9,45], the hydration of  $\text{Ln}$  tungstates decreases their unit-cell volume (7% for  $\text{Y}_2\text{W}_3\text{O}_{12}$  [45]), which leads to smaller lattice parameters and shorter bond lengths. This moves the Raman shift towards higher wavenumbers and increases the intensity of the scattering (Figure 7b).

### 3.5.2. FT-IR Study

FT-IR analysis was applied to identify specific chemical bonds and fragments occurring in the synthesized samples. The freshly prepared amorphous precursor powders demonstrate very similar FT-IR spectra, with three broadened strong peaks around  $824\text{--}832\text{ cm}^{-1}$ ,  $1624\text{--}1627\text{ cm}^{-1}$ , and  $3340\text{--}3360\text{ cm}^{-1}$ , together with several less intense bands at  $\sim 440\text{--}450\text{ cm}^{-1}$ ,  $620\text{--}630\text{ cm}^{-1}$ ,  $920\text{--}930\text{ cm}^{-1}$ , and  $1400\text{--}1415\text{ cm}^{-1}$ , and  $1520\text{--}1530\text{ cm}^{-1}$  (Figure 8a). The spectral features lying in the range of  $400\text{--}1000\text{ cm}^{-1}$  can be assigned to the bending and stretching modes of the  $\text{WO}_x$  moieties, and those in the range of

1623–1625  $\text{cm}^{-1}$  and 3340–3360  $\text{cm}^{-1}$  are due to the bending mode ( $\nu_2$ ) of H–O–H vibrations and longitudinal stretching vibrations of the O–H groups ( $\nu_1$  and  $\nu_3$ ) of the surface-absorbed water molecules, respectively, [26,49–51].

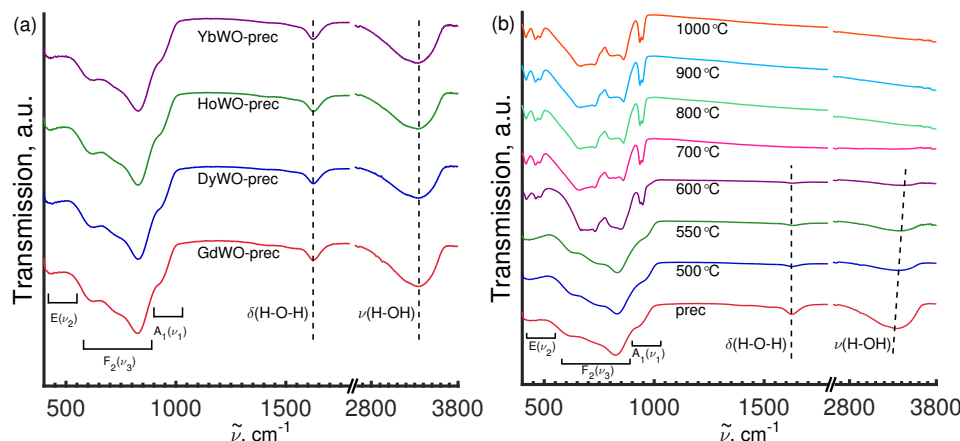


**Figure 8.** FT-IR spectra of  $Ln$  tungstate precursors  $LnWO$ -prec (a),  $Gd_2(WO_4)_3$  samples prepared by the calcination of the precursor at different temperatures (b).

It is observed that the crystallization of  $GdWO$ -600 (monoclinic, sp. gr.  $C12/c1(15)$ ) leads to the appearance in the FT-IR spectrum of intense bands assigned to vibrations of the  $WO_4^{2-}$  groups observed at wavenumbers ranged from 400  $\text{cm}^{-1}$  to 1000  $\text{cm}^{-1}$ . Furthermore, the O–H absorption bands get weaker and eventually disappear due to dehydration (Figure 8b). As it can be seen from Figure 8b, there are virtually no change in the FT-IR spectra of  $Gd_2(WO_4)_3$  for annealing temperatures raised from 700  $^{\circ}\text{C}$  to 1000  $^{\circ}\text{C}$ , which strongly implies that the oxygen sublattice is successfully formed already at 700  $^{\circ}\text{C}$ . The vibrational peaks at around 728  $\text{cm}^{-1}$  and 860  $\text{cm}^{-1}$  are assigned to the O–W–O stretching modes of the  $WO_4^{2-}$  tetrahedron. The 418  $\text{cm}^{-1}$  and 460  $\text{cm}^{-1}$  bands can be attributed to the stretching vibrations of the W–O bonds [52]. It is of note that the FT-IR peaks revealed in the spectra of the well-crystallized  $Gd_2(WO_4)_3$ -1000  $^{\circ}\text{C}$  sample are assigned to the tetrahedral  $W(1)O_4$  and  $W(2)O_4$  units in  $La_2(WO_4)_3$ , which crystallizes in the monoclinic structure (sp. gr.  $C12/c1(15)$ ) as reported by other authors [48].

The FT-IR spectra of heavy  $Ln$  tungstates with the monoclinic structure (sp. gr.  $P12_1/a1(14)$ ) were very different from the spectra of  $Gd_2(WO_4)_3$  (monoclinic, sp. gr.  $C12/c1(15)$ ). Namely, the FT-IR spectra of  $Ho_2(WO_4)_3$  and  $Yb_2(WO_4)_3$  show a significant decrease in the number of peaks, as well as the presence of O–H absorption bands even for well-crystallized samples calcined at 1000  $^{\circ}\text{C}$  (Figure 9). As it can be seen from Figure 9a, the FT-IR spectrum of  $Dy_2(WO_4)_3$  is intermediate between the Gd and (Ho or Yb) tungstates. It contains a large number of absorption bands corresponding to the monoclinic structure, but also it shows O–H absorption bands. This is in a good agreement with STA and X-ray diffraction data that the synthesized sample is a mixture of two monoclinic phases (sp. gr.  $C12/c1(15)$  and (sp. gr.  $P12_1/a1(14)$ ) (see Table S4).

Furthermore, we found that synthesized and quenched in a desiccator  $LnWO$ -1000-desic ( $Ln = Dy, Ho$  and  $Yb$ ) powders reveal very weak vibrational peaks at 1613–1616  $\text{cm}^{-1}$  and 3380–3500  $\text{cm}^{-1}$  of the O–H bonds of the surface-absorbed water molecules (Figures 9 and S5). The FT-IR spectra of  $Dy_2(WO_4)_3$  demonstrate only minute changes during storage in air in the region from 400  $\text{cm}^{-1}$  to 1000  $\text{cm}^{-1}$ , assigned to vibrational modes within the  $WO_4$  tetrahedra in the monoclinic structure (sp. gr.  $C12/c1(15)$ ). The intensity of the O–H absorption modes for sample  $DyWO$ -1000-desic is weaker as compared to sample  $DyWO$ -1000 which is evidently caused by the higher content of the hygroscopic phase (sp. gr.  $P12_1/a1$ ) in the latter (see Table S4). For  $DyWO$ -1000, the intensity of the O–H absorption bands shows a dramatic growth upon air storage (Figure 9a).

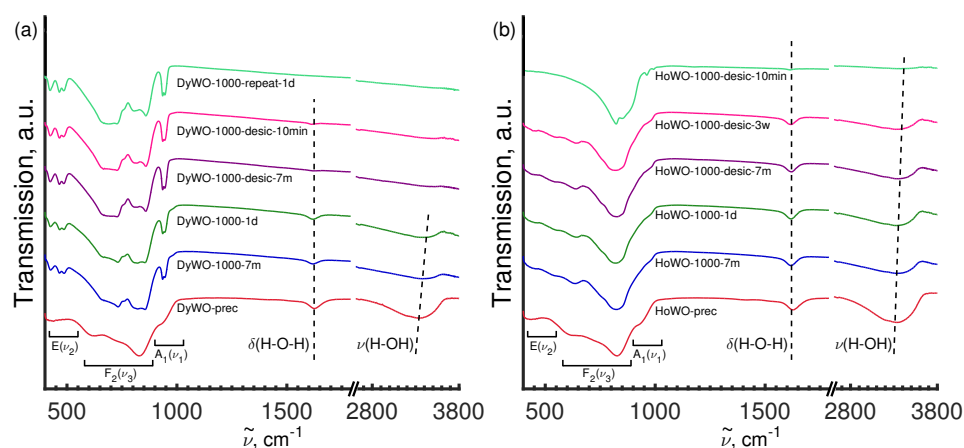


**Figure 9.** FT-IR spectra of  $\text{Dy}_2(\text{WO}_4)_3$  (a) and  $\text{Ho}_2(\text{WO}_4)_3$  (b) powders prepared under different conditions.

The FT-IR spectrum of the as prepared and quenched in a desiccator  $\text{HoWO-1000-desic}$  sample manifests absorption bands at  $823\text{ cm}^{-1}$ ,  $850\text{ cm}^{-1}$  (both asymmetric stretching vibration  $\nu_3$  [43]),  $962\text{ cm}^{-1}$  and  $993\text{ cm}^{-1}$  (both symmetric stretching vibration  $\nu_1$  [43]),  $1614\text{ cm}^{-1}$  (bending vibration of hydrogen bonded OH-group of the water molecule) and  $3377\text{ cm}^{-1}$  (stretching vibration of the OH-group) [26,49–51] (Figure 9b). The hydration of the sample upon storage in air leads to the disappearance of absorption bands at  $850\text{ cm}^{-1}$ ,  $962\text{ cm}^{-1}$  and  $993\text{ cm}^{-1}$ , as well as to a shift in the position of the most intense peak from  $823\text{ cm}^{-1}$  to  $819\text{ cm}^{-1}$ . Disappearance of specific vibrational features in the range typical of internal stretching vibrations within the  $\text{WO}_4$  tetrahedron can be explained assuming that water molecules incorporated in the  $\text{Ln}_2(\text{WO}_4)_3$  framework, block the rocking-type motion of the coordination polyhedra and thus some vibrational bands become silent [9,43]. In addition, a significant increase in the intensity of the O-H absorption bands is observed at  $1618\text{ cm}^{-1}$  and  $3377\text{ cm}^{-1}$ , along with appearance of absorption band at  $640\text{ cm}^{-1}$ , characteristic for libration motion of water molecules [51] (Figure 9b). The FT-IR spectra of  $\text{Yb}_2(\text{WO}_4)_3$  (Figure S5) are similar to that of  $\text{Ho}_2(\text{WO}_4)_3$  and change in a similar way upon storage in air.

The observed differences in the water absorption capacity of Gd and heavy  $\text{Ln}$  ( $\text{Ln} = \text{Dy}, \text{Ho}, \text{Yb}$ ) tungstates may be explained by the structural difference.  $\text{Gd}_2(\text{WO}_4)_3$  (monoclinic, sp. gr.  $\text{C12/c1(15)}$ ) has a closely packed structure due to edge sharing  $\text{GdO}_8$  polyhedra. The heavier  $\text{Ln}$  tungstates (sp. gr.  $\text{P12}_1/\text{a1(14)}$ ) have open structures with corner-sharing  $\text{LnO}_6$  and  $\text{WO}_4$  moieties (with the  $\text{Ln-O-W}$  bridges), which tend to accommodate additional  $\text{H}_2\text{O}$  molecules within empty intraframework cavities (Figure 4).

#### 4. Conclusions

Effects of the lanthanoid cation type and annealing temperature on the phase preference, short- and long-range structures of  $\text{Ln}_2(\text{WO}_4)_3$  tungstates synthesized via the coprecipitation are elucidated in detail with a set of contemporary techniques, including synchrotron radiation-based X-ray diffraction, X-ray absorption spectroscopy, Raman and FT-IR spectroscopy, and simultaneous thermal analysis. The crystallization of initially amorphous precursors is initiated at  $600\text{--}650\text{ }^\circ\text{C}$  to afford crystalline powders with the monoclinic structures of either  $\text{C12/c1(15)}$  for  $\text{Ln} = \text{Gd}$ , and  $\text{Dy}$  or  $\text{P12}_1/\text{a1(14)}$  types for  $\text{Yb}_2(\text{WO}_4)_3$ . For the  $\text{Dy}_2(\text{WO}_4)_3$  sample calcined at  $1000\text{ }^\circ\text{C}$ , an alternative monoclinic structure (sp. gr.  $\text{P12}_1/\text{a1}$ ) emerges, which further becomes the dominant one for  $\text{Ln} = \text{Ho}, \text{Yb}$ . A repeated heating of  $\text{Dy}_2(\text{WO}_4)_3$  to  $1000\text{ }^\circ\text{C}$  induces an irreversible transformation  $\text{P12}_1/\text{a1(14)} \rightarrow \text{C12/c1(15)}$  therein. Meanwhile, holmium and ytterbium tungstates trihydrates  $\text{Ho}_2(\text{WO}_4)_3 \cdot 3\text{H}_2\text{O}$  and  $\text{Yb}_2(\text{WO}_4)_3 \cdot 3\text{H}_2\text{O}$  retain their crystal structures (sp. gr.  $\text{P12}_1/\text{a1(14)}$ ).

The local structure of all well-crystallized compounds is composed of  $Ln^{3+}$  lanthanoid cations and somewhat distorted  $WO_4^{2-}$  anionic tetrahedra. The change in the space group preference of the monoclinic crystalline structure of  $Ln$  tungstates along the series Gd-Dy-Ho-Yb is governed by progressive changes in the  $Ln$ -O coordination shell. The high hygroscopicity of lanthanoid tungstates  $Ln_2(WO_4)_3$  ( $Ln = Dy, Ho, Yb$ ) is rationalized on the basis of structural features of the monoclinic lattice (sp. gr.  $P12_1/a1$ ).

Most essential features of phase preferences and hydration behavior found for heavy lanthanoid tungstates in the present study are summarized in Table 5.

**Table 5.** Summary of structural features of heavy  $Ln$  tungstates under study.

$Ln$ Type	Phase Preference	Comment
Gd	$C12/c1$	Negligible proneness to hydration
Dy	$C12/c1$ , $P12_1/a1$	The $P12_1/a1$ phase component is prone to fast spontaneous hydration. The balance between $C12/c1$ and $P12_1/a1$ can be controlled by preparation protocol: a strictly single-phase $C12/c1$ can be obtained via repeated heating
Ho	$P12_1/a1$	Rapid spontaneous hydration
Yb	$P12_1/a1$ , $Pbcn$	Rapid spontaneous hydration; the $Pbcn$ phase probably corresponds to an unhydrated or partly hydrated structure; fully hydrated samples are single-phase $P12_1/a1$

**Supplementary Materials:** The following supporting information can be downloaded at: <https://www.mdpi.com/article/10.3390/cryst12070892/s1>.

**Author Contributions:** Conceptualization, V.V.P.; methodology, V.V.P.; validation, V.V.P., A.P.M. and Y.V.Z.; formal analysis, A.A.Y., B.R.G., S.G.R. and E.V.K.; investigation, V.V.P., Y.V.Z., S.G.R., F.E.D., R.D.S., E.V.K., N.A.T., N.V.O. and I.V.S.; resources, V.V.P.; data curation, A.A.Y. and B.R.G.; writing—original draft preparation, V.V.P. and Y.V.Z.; writing—review and editing, V.V.P., Y.V.Z. and A.A.I.; visualization, A.A.Y., B.R.G., A.A.I., F.E.D. and E.V.K.; supervision, A.P.M.; project administration, A.P.M.; funding acquisition, A.P.M. All authors have read and agreed to the published version of the manuscript.

**Funding:** This work was supported by the Russian Federation represented by the Ministry of Science and Higher Education of the Russian Federation (Agreement No 075-15-2021-1352).

**Institutional Review Board Statement:** Not applicable.

**Informed Consent Statement:** Not applicable.

**Data Availability Statement:** Data sharing not applicable.

**Acknowledgments:** The authors thank O. N. Seregina, I. G. Rachenok, and K. V. Ponkratov for their help in experiments.

**Conflicts of Interest:** The authors declare no conflict of interest.

## References

1. Imanaka, N.; Köhler, J.; Tamura, S.; Adachi, G. Ion conducting behavior in  $(Lu_{1-x}M_x)_2(WO_4)_3$  solid solutions ( $M = Sm, Ho, Er$ ) with the  $Sc_2(WO_4)_3$  type structure. *Eur. J. Inorg. Chem.* **2002**, *1*, 105–109. [CrossRef]
2. Zhou, Y.; Yan, B.  $RE_2(MO_4)_3 \cdot Ln^{3+}$  ( $RE = Y, La, Gd, Lu$ ;  $M = W, Mo$ ;  $Ln = Eu, Sm, Dy$ ) microcrystals: controlled synthesis, microstructure and tunable luminescence. *CrystEngComm* **2013**, *15*, 5694. [CrossRef]
3. Kaczmarek, A.M.; Deun, R.V. Rare earth tungstate and molybdate compounds—From 0D to 3D architectures. *Chem. Soc. Rev.* **2013**, *42*, 8835–8848. [CrossRef]
4. Liu, J.; Kaczmarek, A.; Deun, R. Advances in tailoring luminescent rare-earth mixed inorganic materials. *Chem. Soc. Rev.* **2018**, *47*, 7225–7238. [CrossRef]



5. Vickery, R.C. Studies of the rare-earth tungstates. *J. Chem. Soc.* **1949**, 2501–2505. [\[CrossRef\]](#)
6. Borchardt, H. Rare Earth Tungstates and 1:1 Oxytungstates. *J. Chem. Phys.* **1963**, 39, 504–511. [\[CrossRef\]](#)
7. Nassau, K.; Levinstein, H.J.; Loiacono, G.M. A comprehensive study of trivalent tungstates and molybdates of the type  $L_2(MO_4)_3$ . *J. Phys. Chem. Solids* **1965**, 26, 1805–1816. [\[CrossRef\]](#)
8. Sleight, A.W. Negative Thermal Expansion. *MRS Proc.* **2002**, 755, 106. [\[CrossRef\]](#)
9. Sumithra, S.; Umarji, A.M. Role of crystal structure on the thermal expansion of  $Ln_2W_3O_{12}$  ( $Ln = La, Nd, Dy, Y, Er$  and  $Yb$ ). *Solid State Sci.* **2004**, 6, 1313–1319. [\[CrossRef\]](#)
10. Liu, H.; Sun, W.; Zhang, Z.; Lovings, L.; Lind, C. Thermal Expansion Behavior in the  $A_2M_3O_{12}$  Family of Materials. *Solids* **2021**, 2, 87–107. [\[CrossRef\]](#)
11. Marinkovic, B.A.; Pontón, P.I.; Romao, C.P.; Moreira, T.; White, M.A. Negative and Near-Zero Thermal Expansion in  $A_2M_3O_{12}$  and Related Ceramic Families: A Review. *Front. Mater.* **2021**, 8, 741560. [\[CrossRef\]](#)
12. Templeton, D.H.; Zalkin, A. Crystal structure of europium tungstate. *Acta Cryst.* **1963**, 16, 762–766. [\[CrossRef\]](#)
13. Gärtner, M.; Abeln, D.; Pring, A.; Wilde, M.; Reller, A. Synthesis, Structure, and Reactivity of Novel Lanthanum Tungstates. *J. Solid State Chem.* **1994**, 111, 128–133. [\[CrossRef\]](#)
14. Gressling, T.; Müller-Buschbaum, H. Zur Kristallstruktur von  $Ce_2(WO_4)_3$ /On the Crystal Structure of  $Ce_2(WO_4)_3$ . *Z. Naturforsch. B* **1995**, 50, 1513–1516. [\[CrossRef\]](#)
15. Shen, R.; Wang, C.; Wang, T.; Dong, C.; Chen, X.; Liang, J. Crystal Structures of  $Dy_2(WO_4)_3$  and  $GdY(WO_4)_3$ . *Rare Met.* **2003**, 22, 49–54.
16. Weil, M.; Stöger, B.; Aleksandrov, L.  $Nd_2(WO_4)_3$ . *Acta Crystallogr. E* **2009**, 65, i45. [\[CrossRef\]](#)
17. dos Passos, R.H.D.; de Souza, C.P.; Bernard-Nicod, C.; Leroux, C.; Arab, M. Structural and electrical properties of cerium tungstate: Application to methane conversion. *Ceram. Int.* **2020**, 46, 8021–8030. [\[CrossRef\]](#)
18. Sabalisk, N.P.; de Cos, G.G.; González-Silgo, C.; Guzmán-Afonso, C.; Lavín, V.; López-Solano, J.; Martín-Mateos, I.T.; Mestres, L.; Mujica, A.; Santamaría-Pérez, D.; et al. Role of rare earth sites and vacancies in the anomalous compression of modulated scheelite tungstates  $RE_2(WO_4)_3$ . *Phys. Rev. Mater.* **2021**, 5, 123601. [\[CrossRef\]](#)
19. Pestereva, N.N.; Vyatkin, I.A.; Lopatin, D.A.; Guseva, A.F. Nature of ionic conductivity of lanthanoid tungstates with imperfect scheelite structure. *Russ. J. Electrochem.* **2016**, 52, 1082–1089. [\[CrossRef\]](#)
20. Xiao, X.; Cheng, Y.; Peng, J.; Wu, M.; Chen, D.; Hu, Z.; Kiyanagi, R.; Fieramosca, J.; Short, S.; Jorgensen, J. Thermal expansion properties of  $A_2(MO_4)_3$  ( $A = Ho$  and  $Tm$ ;  $M = W$  and  $Mo$ ). *Solid State Sci.* **2008**, 10, 321–325. [\[CrossRef\]](#)
21. Lahoz, F.; Sabalisk, N.P.; Cerdeiras, E.; Mestres, L. Nano-to millisecond lifetime luminescence properties in  $Ln_2(WO_4)_3$  ( $Ln = La, Ho, Tm$  and  $Eu$ ) microcrystalline powders with different crystal structures. *J. Alloys Compd.* **2015**, 649, 1253–1259. [\[CrossRef\]](#)
22. Kol'tsova, T.N. X-ray diffraction study of  $Y_2W_3O_{12} \cdot 3H_2O$ . *Inorg. Mater.* **2001**, 37, 1175–1177. [\[CrossRef\]](#)
23. Pontón, P.I.; Prisco, L.P.; Dosen, A.; Faro, G.S.; de Abreu, M.A.; Marinkovic, B.A. Co-precipitation synthesis of  $Y_2W_3O_{12}$  submicronic powder. *Ceram. Int.* **2017**, 43, 4222–4228. [\[CrossRef\]](#)
24. Yamazoe, S.; Hitomi, Y.; Shishido, T.; Tanaka, T. XAFS Study of Tungsten  $L_{1-}$  and  $L_{3-}$  Edges: Structural Analysis of  $WO_3$  Species Loaded on  $TiO_2$  as a Catalyst for Photo-oxidation of  $NH_3$ . *J. Phys. Chem. C* **2008**, 112, 6869–6879. [\[CrossRef\]](#)
25. Timoshenko, J.; Anspoks, A.; Kalinko, A.; Kuzmin, A. Local structure of nanosized tungstates revealed by evolutionary algorithm. *Phys. Status Solidi A* **2015**, 212, 265–273. [\[CrossRef\]](#)
26. Kuriakose, S.; H, H.; Jose, A.; John, M.; Varghese, T. Structural and optical characterization of lanthanum tungstate nanoparticles synthesized by chemical precipitation route and their photocatalytic activity. *Opt. Mater.* **2020**, 99, 109571. [\[CrossRef\]](#)
27. Meng, Q.; Hua, R.; Chen, B.; Tian, Y.; Lu, S.; Sun, L. Study on Luminescent Properties of  $Eu^{3+}$  Doped  $Gd_2WO_6$ ,  $Gd_2W_2O_9$  and  $Gd_2(WO_4)_3$  Nanophosphors Prepared by Co-Precipitation. *J. Nanosci. Nanotechnol.* **2011**, 11, 182–188. [\[CrossRef\]](#)
28. Popov, V.V.; Menushenkov, A.P.; Yaroslavtsev, A.A.; Zubavichus, Y.V.; Gaynanov, B.R.; Yastrebtsev, A.A.; Leshchev, D.S.; Chernikov, R.V. Fluorite-pyrochlore phase transition in nanostructured  $Ln_2Hf_2O_7$  ( $Ln = La-Lu$ ). *J. Alloys Compd.* **2016**, 689, 669–679. [\[CrossRef\]](#)
29. Popov, V.V.; Menushenkov, A.P.; Gaynanov, B.R.; Zubavichus, Y.V.; Svetogorov, R.D.; Yastrebtsev, A.A.; Pisarev, A.A.; Arzhatkina, L.A.; Ponkratov, K.V. Features of formation and evolution of crystal and local structures in nanocrystalline  $Ln_2Zr_2O_7$  ( $Ln = La-Tb$ ). *J. Phys. Conf. Ser.* **2017**, 941, 012079. [\[CrossRef\]](#)
30. Popov, V.V.; Menushenkov, A.P.; Ivanov, A.A.; Gaynanov, B.R.; Yastrebtsev, A.A.; d'Acapito, F.; Puri, A.; Castro, G.R.; Shchetinin, I.V.; Zheleznyi, M.V.; et al. Comparative analysis of long- and short-range structures features in titanates  $Ln_2Ti_2O_7$  and zirconates  $Ln_2Zr_2O_7$  ( $Ln = Gd, Tb, Dy$ ) upon the crystallization process. *J. Phys. Chem. Solids* **2019**, 130, 144–153. [\[CrossRef\]](#)
31. Popov, V.V.; Menushenkov, A.P.; Yastrebtsev, A.A.; Molokova, A.Y.; Rudakov, S.G.; Svetogorov, R.D.; Tsarenko, N.A.; Ponkratov, K.V.; Ognevskaya, N.V.; Seregina, O.N. The effect of the synthesis conditions on the structure and phase transitions in  $Ln_2(MoO_4)_3$ . *Solid State Sci.* **2021**, 112, 106518. [\[CrossRef\]](#)
32. Popov, V.V.; Menushenkov, A.P.; Yastrebtsev, A.A.; Rudakov, S.G.; Ivanov, A.A.; Gaynanov, B.R.; Svetogorov, R.D.; Khramov, E.V.; Zubavichus, Y.V.; Molokova, A.Y.; et al. Multiscale study on the formation and evolution of the crystal and local structures in lanthanoid tungstates  $Ln_2(WO_4)_3$ . *J. Alloys Compd.* **2022**, 910, 164922. [\[CrossRef\]](#)
33. Svetogorov, R.D.; Dorovatovskii, P.V.; Lazarenko, V.A. Belok/XSA Diffraction Beamline for Studying Crystalline Samples at Kurchatov Synchrotron Radiation Source. *Cryst. Res. Tech.* **2020**, 55, 1900184. [\[CrossRef\]](#)
34. Petricek, V.; Dusek, M.; Palatinus, L. Crystallographic computing system JANA2006: General features. *Z. Krist.* **2014**, 229, 345–352. [\[CrossRef\]](#)

35. Chernyshov, A.; Veligzhanin, A.; Zubavichus, Y. Structural Materials Science end-station at the Kurchatov Synchrotron Radiation Source: Recent instrumentation upgrades and experimental results. *Nucl. Instrum. Methods Phys. Res. Sect. A* **2009**, *603*, 95–98. [\[CrossRef\]](#)
36. Ravel, B.; Newville, M. ATHENA, ARTEMIS, HEPHAESTUS: Data analysis for X-ray absorption spectroscopy using IFEFFIT. *J. Synchrotron Radiat.* **2005**, *12*, 537–541. [\[CrossRef\]](#)
37. Newville, M. IFEFFIT: Interactive XAFS analysis and FEFF fitting. *J. Synchrotron Radiat.* **2001**, *8*, 322–324. [\[CrossRef\]](#)
38. Rehr, J.J.; Albers, R.C. Theoretical approaches to X-ray absorption fine structure. *Rev. Mod. Phys.* **2000**, *72*, 621–654. [\[CrossRef\]](#)
39. Klementev, K.V. Extraction of the fine structure from X-ray absorption spectra. *J. Phys. D Appl. Phys.* **2001**, *34*, 209–217. [\[CrossRef\]](#)
40. Rehr, J.J.; Kas, J.J.; Vila, F.D.; Prange, M.P.; Jorissen, K. Parameter-free calculations of X-ray spectra with FEFF9. *Phys. Chem. Chem. Phys.* **2010**, *12*, 5503–5513. [\[CrossRef\]](#)
41. Evdokimov, A.A.; Efremov, V.A.; Trunov, V.K.; Kleinman, I.A.; Dzurinskii, B.F. *Rare Earth Elements Compounds. Molybdates, Tungstates*; Nauka (Science): Moscow, Russia, 1991. (In Russian)
42. Wu, M.Y.; Jia, Y.; Sun, Q. Effects of  $A^{3+}$  cations on hydration in  $A_2M_3O_{12}$  family materials: A first-principles study. *Comput. Mater. Sci.* **2016**, *111*, 28–33. [\[CrossRef\]](#)
43. Shmurak, S.Z.; Kedrov, V.V.; Kiselev, A.P.; Fursova, T.N.; Zver'kova, I.I.; Khasanov, S.S. Spectral and Structural Characteristics of  $(Lu_{1-x}Eu_x)_2(WO_4)_3$  Tungstates. *Phys. Solid State* **2019**, *61*, 2117–2129. [\[CrossRef\]](#)
44. Richard, A.P.; Edwards, D.D. Subsolidus phase relations and crystal structures of the mixed-oxide phases in the  $In_2O_3-WO_3$  system. *J. Solid State Chem.* **2004**, *177*, 2740–2748. [\[CrossRef\]](#)
45. Sumithra, S.; Umarji, A.M. Hygroscopicity and bulk thermal expansion in  $Y_2W_3O_{12}$ . *Mater. Res. Bull.* **2005**, *40*, 167–176. [\[CrossRef\]](#)
46. Luo, Q.H.; Howell, R.C.; Dankova, M.; Bartis, J.; Williams, C.W.; Horrocks, W.D.; Young, V.G.; Rheingold, A.L.; Francesconi, L.C.; Antonio, M.R. Coordination of Rare-Earth Elements in Complexes with Monovacant Wells–Dawson Polyoxoanions. *Inorg. Chem.* **2001**, *40*, 1894–1901. [\[CrossRef\]](#)
47. Sabalisk, N.P.; Lopez-Solano, J.; Guzman-Afonso, C.; Santamaria-Perez, D.; Gonzalez-Silgo, C.; Mujica, A.; Munoz, A.; Rodriguez-Hernandez, P.; Radescu, S.; Vendrell, X.; et al. Effect of pressure on  $La_2(WO_4)_3$  with a modulated scheelite-type structure. *Phys. Rev. B* **2014**, *89*, 174112. [\[CrossRef\]](#)
48. Burcham, L.J.; Wachs, I.E. Vibrational analysis of the two non-equivalent, tetrahedral tungstate ( $WO_4$ ) units in  $Ce_2(WO_4)_3$  and  $La_2(WO_4)_3$ . *Spectrochim. Acta A* **1998**, *54*, 1355–1368. [\[CrossRef\]](#)
49. Pourmortazavi, S.M.; Rahimi-Nasrabadi, M.; Ganjali, M.; Sadeghpour, K.M.; Norouzi, P.; Faridbod, F. Facile and Effective Synthesis of Praseodymium Tungstate Nanoparticles through an Optimized Procedure and Investigation of Photocatalytic Activity. *Open Chem. J.* **2017**, *15*, 129–138. [\[CrossRef\]](#)
50. Rahimi-Nasrabadi, M.; Pourmortazavi, S.M.; Ganjali, M.R.; Banan, A.R.; Ahmadi, F. Synthesis procedure optimization and characterization of europium (III) tungstate nanoparticles. *J. Mol. Struct.* **2014**, *1074*, 85–91. [\[CrossRef\]](#)
51. Nakamoto, K. *Infrared and Raman Spectra of Inorganic and Coordination Compounds. Part A: Theory and Applications in Inorganic Chemistry*, 6th ed.; John Wiley & Sons, Inc.: Hoboken, NJ, USA, 2009.
52. Yin, M.; Liu, Y.; Mei, L.; Molokeev, M.S.; Huang, Z.; Fang, M. Preparation, crystal structure and up-conversion luminescence of  $Er^{3+}$ ,  $Yb^{3+}$  co-doped  $Gd_2(WO_4)_3$ . *RSC Adv.* **2015**, *5*, 73077–73082. [\[CrossRef\]](#)